NANO LETTERS

pubs.acs.org/NanoLett Letter

Elucidating Piezoelectricity and Strain in Monolayer MoS_2 at the Nanoscale Using Kelvin Probe Force Microscopy

Alex C. De Palma, Xinyue Peng, Saba Arash, Frank Y. Gao, Edoardo Baldini, Xiaoqin Li, and Edward T. Yu*

Cite This: *Nano Lett.* 2024, 24, 1835−1842 Read Online

ACCESS | Metrics & More | Article Recommendations | Supporting Information

ABSTRACT: Strain engineering modifies the optical and electronic properties of atomically thin transition metal dichalcogenides. Highly inhomogeneous strain distributions in two-dimensional materials can be easily realized, enabling control of properties on the nanoscale; however, methods for probing strain on the nanoscale remain challenging. In this work, we characterize inhomogeneously strained monolayer MoS_2 via Kelvin probe force microscopy and electrostatic gating, isolating the contributions of strain from other electrostatic effects and enabling the measurement of all components of the two-dimensional strain tensor on length scales less than 100 nm. The combination of these methods is used to calculate the spatial distribution of the electrostatic potential resulting from piezoelectricity, presenting a powerful way to characterize inhomogeneous strain and piezoelectricity that can be extended toward a variety of 2D materials.

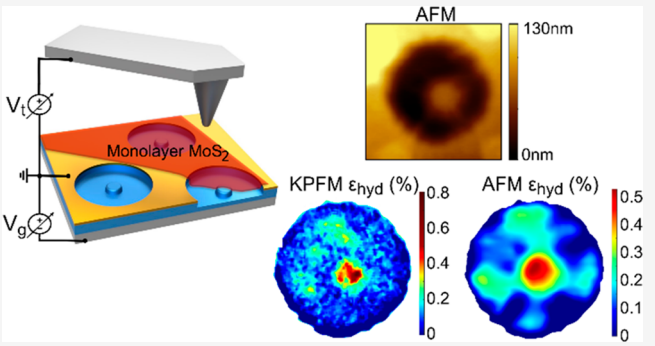

KEYWORDS: *2D materials, transition metal dichalcogenides, strain, piezoelectricity, Kelvin probe force microscopy*

Atomically thin semiconducting transition metal dichalcogenides (TMDs) are widely studied due to their novel properties enabling applications in electronic and optoelectronic devices.[1−4] Strain in atomically thin TMDs has been used as a tool for modifying optical and electronic properties, and the ability of TMDs to withstand large deformations before rupture enables large modifications of properties such as the bandgap energy.[5−8] In particular, localized, inhomogeneous strain is relevant to many phenomena, such as exciton funneling and single photon quantum emission, and can be easily realized on the nanoscale in atomically thin materials using a variety of techniques such as indentation, bubbles, and nanopatterned substrates.[9−18] Piezoelectric and other electromechanical coupling effects can also arise in the presence of inhomogeneous strain distributions in TMDs and other 2D materials.[19−24] Characterizing the strain distribution and piezoelectricity is critical for progress in strain engineering applications in 2D TMDs. Transmission electron microscopy (TEM) can also be used to measure the strain in 2D materials but requires the preparation of thin samples for electron transmission.[25] Optical methods are often used to characterize strain distributions, but these techniques are limited in spatial resolution by the diffraction limit associated with optical illumination and detection.[9,15,16,26−28] While the resulting approximations can give a good estimation of the broad features of a strain distribution, these techniques cannot directly observe highly localized strain often present in real experiments due to contributions from edges, roughness, ripples, and other sources of nonidealities. Near-field optical methods using scanning probe microscopy can be used to resolve localized strain with spatial resolution below the diffraction limit but require a combination of scanned probe microscopy instrumentation with optics to align a laser to a metallic SPM probe tip.[14,29]

In this work, we demonstrate a method for probing spatial inhomogeneities in the electronic structure of monolayer MoS_2 due to strain on the nanoscale using Kelvin probe force microscopy (KPFM). KPFM has previously been used to characterize strain in monolayer TMDs, but a complete understanding of the relationship between surface potential and strain has not been developed.[30−32] Using electrostatic gating, we controlled the carrier concentration, probing different regimes of screening and band filling in MoS_2 strained by dielectric nanomesas. Different regimes yield different KPFM contrast, which we attribute to separate mechanisms of strain-induced band structure shifts and piezoelectricity, providing a quantitative characterization of

Received: August 17, 2023
Revised: January 29, 2024
Accepted: February 1, 2024
Published: February 5, 2024

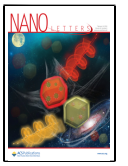

https://doi.org/10.1021/acs.nanolett.3c03100
Nano Lett. 2024, 24, 1835−1842

both. We demonstrate a method to image the spatial distribution of the conduction band edge energy and infer from this the spatial distribution of in-plane hydrostatic strain. Additionally, we present a method for calculating the spatial distribution of the full 2D strain tensor from the in-plane hydrostatic strain distribution. This full strain tensor is used to calculate a piezoelectric-bound charge and potential distribution that agree well with KPFM measurements. This analysis can help to elucidate the mechanisms driving various optical and electronic phenomena occurring in atomically thin TMDs at the nanoscale by allowing for more precise characterization of strain and related properties.

Samples were fabricated to enable electrostatic gating of inhomogeneously strained MoS_2 (Supporting Information Sections S1 and S2), as shown in Figure 1. A gate electrode

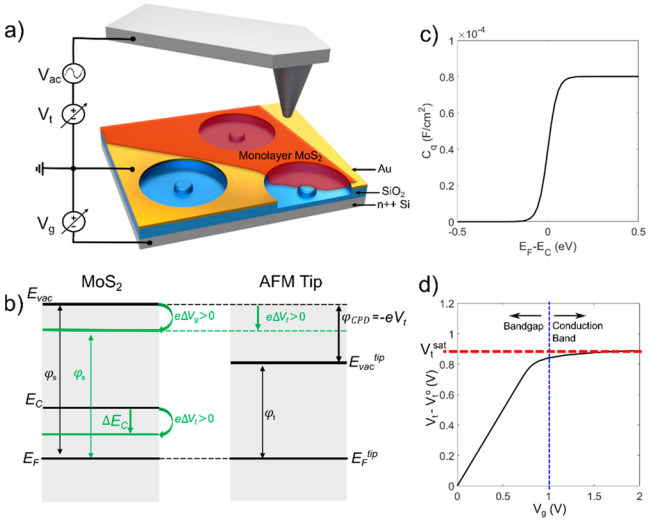

Figure 1. (a) Measurement setup and sample structure. A bottom gate electrode and top ground electrode allow for electrostatic gating to be performed during KPFM measurements. A MoS_2 monolayer is transferred onto a sample of patterned dielectric nanomesas. Voltage V_{ac} and V_t are applied to the tip to characterize electrostatic potential variations over the sample. (b) A schematic of the influence of V_g on the electrostatics of the KPFM measurement, showing the relative alignment of the energy levels in the tip and sample before KPFM feedback is applied, that is, before the application of V_t. The green lines and symbols depict a shift in the energy levels relative to the black lines and symbols for positive V_g. (c) The calculated dependence of C_q on $E_F - E_C$ for monolayer MoS_2 at $T = 300$ K. (d) The calculated dependence of V_t on V_g, assuming E_F is in the midgap at $V_g = 0$ V. V_t shifts by a constant, $V_t^o = -V_{CPD}$, depending on the work function difference between the tip and sample. The red dashed line depicts the approximate position of V_t^{sat}, and the blue dashed line depicts the approximate value of V_g beyond which $E_F \approx E_C$ and $V_t \approx V_t^{sat}$.

consisting of n^{++} Si is separated from a Au top electrode by a SiO_2 gate dielectric. A hexagonal array of holes in the Au layer defines gated areas for study. Dielectric circular nanomesas ~60 nm tall and 500 nm in diameter with relatively flat tops were etched from the SiO_2, providing a source of inhomogeneous strain for monolayer MoS_2. Monolayer MoS_2 was exfoliated from a bulk 2H crystal and transferred to a sample substrate for characterization. In the locations analyzed here, the monolayer is approximately conformal, with some tenting at the mesa edges, to the profile of the hole and mesa (Supporting Information Section S3).

We employ frequency modulated KPFM to map unique electrical information with ~20−100 nm resolution[33] (Supporting Information Section S4). The tip and sample form two electrodes of a capacitor system characterized by a contact potential difference, V_{cpd}, generated by the work function difference between the tip, φ_t, and sample, φ_s, according to $V_{cpd} = \frac{\varphi_s - \varphi_t}{e}$, where e is the fundamental electric charge magnitude. A DC bias voltage, V_t, combined with an AC bias modulation, V_{ac}, with frequency ω are applied to the tip, inducing an electrostatic force F with gradient $\partial F/\partial z$ between the tip and sample with multiple harmonic components:[33]

$$F = F_{dc} + F_\omega + F_{2\omega} \tag{1}$$

$$\frac{\partial F_{dc}}{\partial z} = \frac{1}{2}\frac{\partial^2 C}{\partial z^2}(V_t + V_{cpd})^2 + \frac{1}{4}\frac{\partial C}{\partial z}V_{ac}^2 \tag{2}$$

$$\frac{\partial F_\omega}{\partial z} = \frac{\partial^2 C}{\partial z^2}(V_t + V_{cpd})V_{AC}\sin(\omega t) \tag{3}$$

$$\frac{\partial F_{2\omega}}{\partial z} = -\frac{1}{4}\frac{\partial^2 C}{\partial z^2}V_{ac}^2\cos(2\omega t) \tag{4}$$

where F_{dc}, F_ω, and $F_{2\omega}$ are the force components at zero, ω, and 2ω frequency. V_{cpd} is determined by finding the value of V_t which eliminates the F_ω component of the force, i.e., $V_t = -V_{cpd}$. The amplitude of the $\partial F_{2\omega}/\partial z$ signal in eq 4, $A_{2\omega}$, can also be monitored for a qualitative measurement of the second z-derivative of the tip−sample capacitance, $\partial^2 C/\partial z^2$.

Applying a nonzero V_g in the presence of MoS_2 modulates the work function of MoS_2 and therefore V_t measured in KPFM, as illustrated in Figure 1b. Tuning V_g also shifts the energy levels of the electronic subbands of MoS_2.

In the presence of the monolayer, the relationship between V_g and V_t is dependent on the quantum capacitance, C_q, of MoS_2. C_q is defined as the variation of electric charge with respect to chemical potential, which is related to the density of states (DOS) in the monolayer.[34] This capacitance acts in series with the gate oxide capacitance, C_{ox}, such that the change of V_t due to V_g is given by

$$\frac{dV_t}{dV_g} = \frac{1}{\frac{C_q}{C_{ox}} + 1} \tag{5}$$

The slope dV_t/dV_g depends on the ratio between C_q and C_{ox}. When $C_q = 0$, $dV_t/dV_g = 1$, and when $C_q \gg C_{ox}$, $dV_t/dV_g \sim 0$. The DOS and C_q have been characterized using gated KPFM measurements in a variety of other low-dimensional systems, including thin films of semiconducting organic molecules,[35] InAs nanowires,[36] and graphene.[37]

The theoretical dependence of C_q on $E_F - E_C$ in monolayer MoS_2 is shown in Figure 1c (Supporting Information Section S5). When E_F is in the bandgap, $C_q \sim 0$. As E_F approaches E_C, C_q approaches a maximal value $C_q = q^2 g_{2D}$, where g_{2D} is the 2D DOS at the conduction band edge. The value of g_{2D} for monolayer MoS_2 is $\sim 5 \times 10^{14}$ eV^{-1}cm^{-2},[38] leading to a maximum $C_q \sim 8 \times 10^{-5}$ F/cm^2 near E_C,[39] which is orders of magnitude larger than C_{ox} ($\sim 2-4 \times 10^{-8}$ F/cm^2). Hence, there are two regimes: a regime in which E_F is within the bandgap where $C_q \ll C_{ox}$ and a regime with E_F near E_C where $C_q \gg C_{ox}$.

https://doi.org/10.1021/acs.nanolett.3c03100
Nano Lett. 2024, 24, 1835−1842

Altering V_g transitions between these two regimes by changing the relative positions of E_F and E_C, as illustrated in Figure 1b,c. The regimes of low and high C_q are reflected in the theoretical dependence of V_t on V_g for monolayer MoS_2 in our experiment, as shown in Figure 1d (Supporting Information S5). Increasing V_g increases V_t and C_q. At sufficiently positive V_g, dV_t/dV_g approaches 0, and V_t reaches an approximate saturated value, V_t^{sat}.

A KPFM measurement of topography and surface potential for strained monolayer MoS_2 at $V_g = 0$ V is shown in Figure 2.

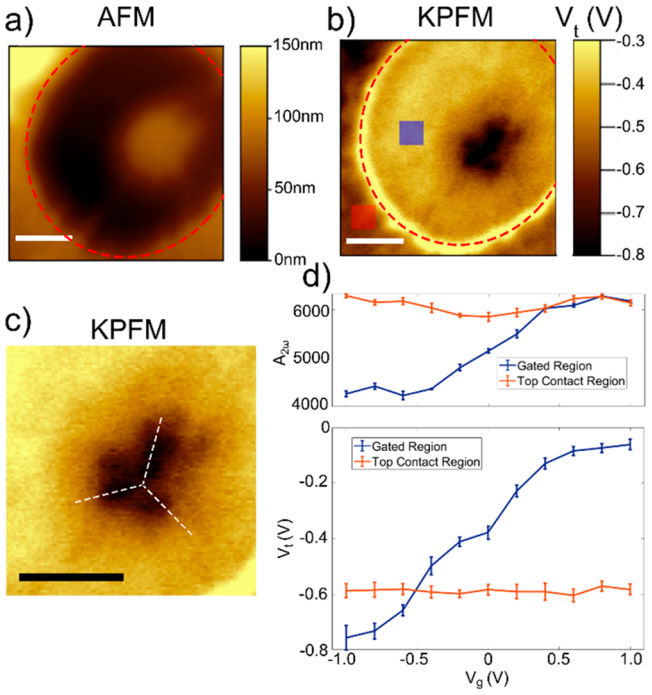

Figure 2. KPFM characterization of strained MoS_2 at $V_g = 0$ V. (a) Topography and (b) V_t. The gated SiO_2 region is within the red circle, and outside of this perimeter is the region of the top Au contact. (c) Closeup of the KPFM image shown in (b). The white dashed lines highlight the 3-fold symmetry seen in the KPFM image. The scale bars in (a)−(c) correspond to 500 nm. (d) The dependence of V_t and $A_{2\omega}$ on V_g. Quantities for the gated region and top contact region are averaged over the areas shaded in blue and red, respectively, in (b). Error bars correspond to 1 standard deviation.

V_t is more negative, corresponding to a larger φ_s, in proximity to the nanomesa, consistent with tensile strain in monolayer MoS_2.[40,41] As highlighted in Figure 2c, this region of contrast has a roughly 3-fold rotational symmetry absent from the underlying topography (Figure 2a), a feature which will be investigated further in subsequent sections.

KPFM characterization of the monolayer as a function of V_g is shown in Figure 2d, demonstrating a similar dependence of V_t on V_g as the theoretical calculations in Figure 1d. The slope within the bandgap deviates from the ideal value of 1, indicating a nonzero DOS within the bandgap of MoS_2 potentially originating from defects and states due to the SiO_2 interface.[39,42,43] Increasing V_g increases $A_{2\omega}$, which we attribute to increasing DOS in the monolayer as E_F approaches E_C, consequently increasing the tip−sample capacitance,[37] and thereby $\partial^2 C/\partial z^2$. For $V_g > 0.6$ V, V_t and $A_{2\omega}$ begin to level off due to the large DOS and C_q as E_F approaches E_C. V_t approaches a saturated value, $V_t^{sat} \approx -50$ mV.

The spatial variation of V_t^{sat} acquired via KPFM is related to the relative position of E_C due to strain. With application of a sufficiently large positive V_g, $V_t = V_t^{sat}$ and $E_F \sim E_C$. The spatial variation in the KPFM image, ΔV_t^{sat}, is then given by

$$\Delta V_t^{sat} = -\frac{\Delta(E_{vac} - E_F)}{e} \approx -\frac{\Delta(E_{vac} - E_C)}{e} \quad (6)$$

where Δ denotes the spatial variation of the quantities. The quantity $\Delta(E_{vac} - E_C)$ is directly related to the strain-induced changes in the conduction band edge energy in monolayer MoS_2. Electrostatic potential variations have an effect equivalent to shifting V_g, but since dV_t/dV_g is small provided that $C_q \gg C_{ox}$, the effect on the measured V_t^{sat} is very small. Therefore, ΔV_t^{sat} is predominantly due to the spatial variation in E_C due to strain.

Based on this analysis, we measure the spatial distribution of $V_t^{sat} \approx -\Delta(E_{vac} - E_C)/e$ via application of a +5 V gate bias. Figure 3a,b shows the transition of KPFM contrast between V_g

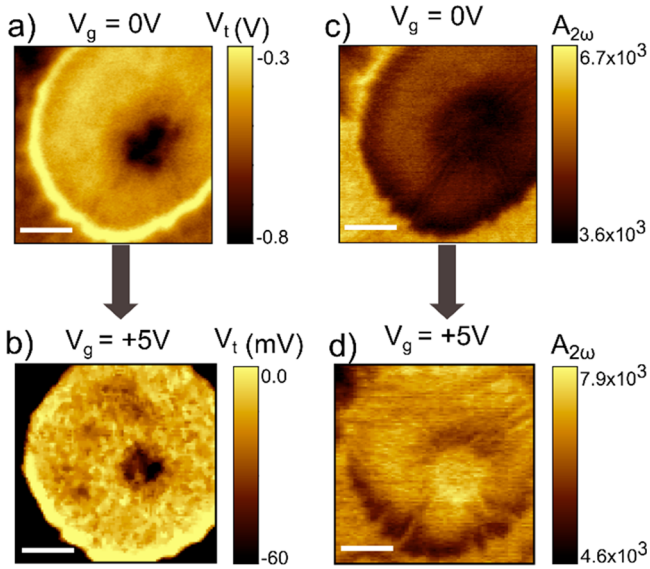

Figure 3. KPFM measurements of (a) V_t at $V_g = 0$ V, (b) V_t at $V_g = 5$ V, (c) $A_{2\omega}$ at $V_g = 0$ V, and (d) $A_{2\omega}$ at $V_g = 5$ V. The color bar scale in (b) was chosen to highlight the contrast within the circular area. V_t outside of the circular area is roughly −0.6 V. The scale bars in all KPFM images correspond to 500 nm.

= 0 V and $V_g = 5$ V in the gated MoS_2 monolayer. Application of the +5 V gate bias alters the spatial variations in V_t; in particular, the spatial distribution of V_t loses the 3-fold symmetry present at $V_g = 0$ and becomes more radially symmetric. $A_{2\omega}$ increases over the gated area at $V_g = 5$ V (Figure 3c,d), implying a large $\partial^2 C/\partial z^2$ and therefore large DOS of the monolayer, indicating that the KPFM measurement at $V_g = 5$ V corresponds to $V_t = V_t^{sat}$. The area over the nanomesa has a more negative V_t than the flat area, consistent with the lowering of E_C relative to E_{vac} in the MoS_2 due to tensile strain. The magnitude of variations in V_t is significantly decreased at $V_g = 5$ V compared to $V_g = 0$ V. These observations suggest that the KPFM contrast at $V_g = 0$ has a significant electrostatic component other than strain, due in part to piezoelectricity, which will be discussed further in subsequent sections.

https://doi.org/10.1021/acs.nanolett.3c03100
Nano Lett. 2024, 24, 1835−1842

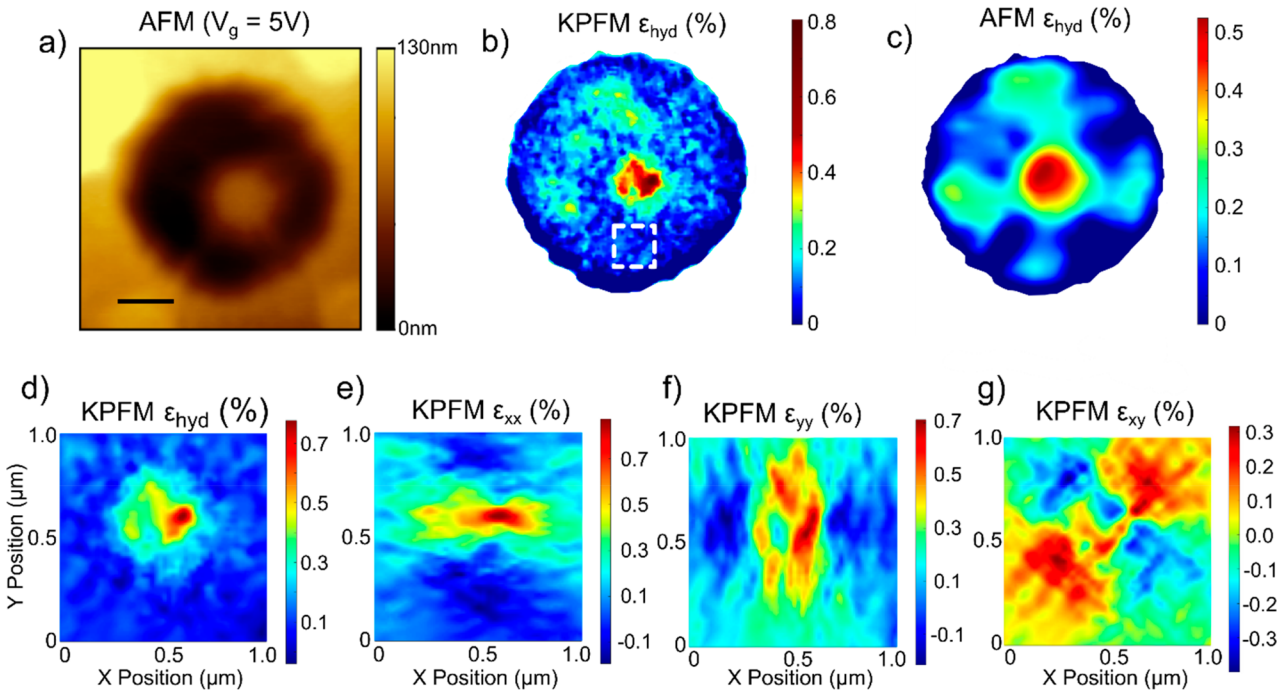

Figure 4. (a) Topography of the MoS_2 on the nanomesa at V_g = 5 V. The scale bar is 500 nm. (b) The in-plane hydrostatic strain determined from the KPFM measurements at V_g = 5 V and the strain deformation potentials of MoS_2. Zero strain was assumed from the average of V_t in the region shown in the dashed white box. (c) The in-plane hydrostatic strain determined from topography in (a). Only the circular region of the gated area is shown, as V_t does not correlate to the strain outside of this area due to the presence of the top Au contact. (d) Zoomed in view of the KPFM-derived hydrostatic strain in proximity to the nanomesa. (e),(f),(g) ε_{xx}, ε_{yy}, ε_{xy} elements of the strain tensor derived from KPFM data.

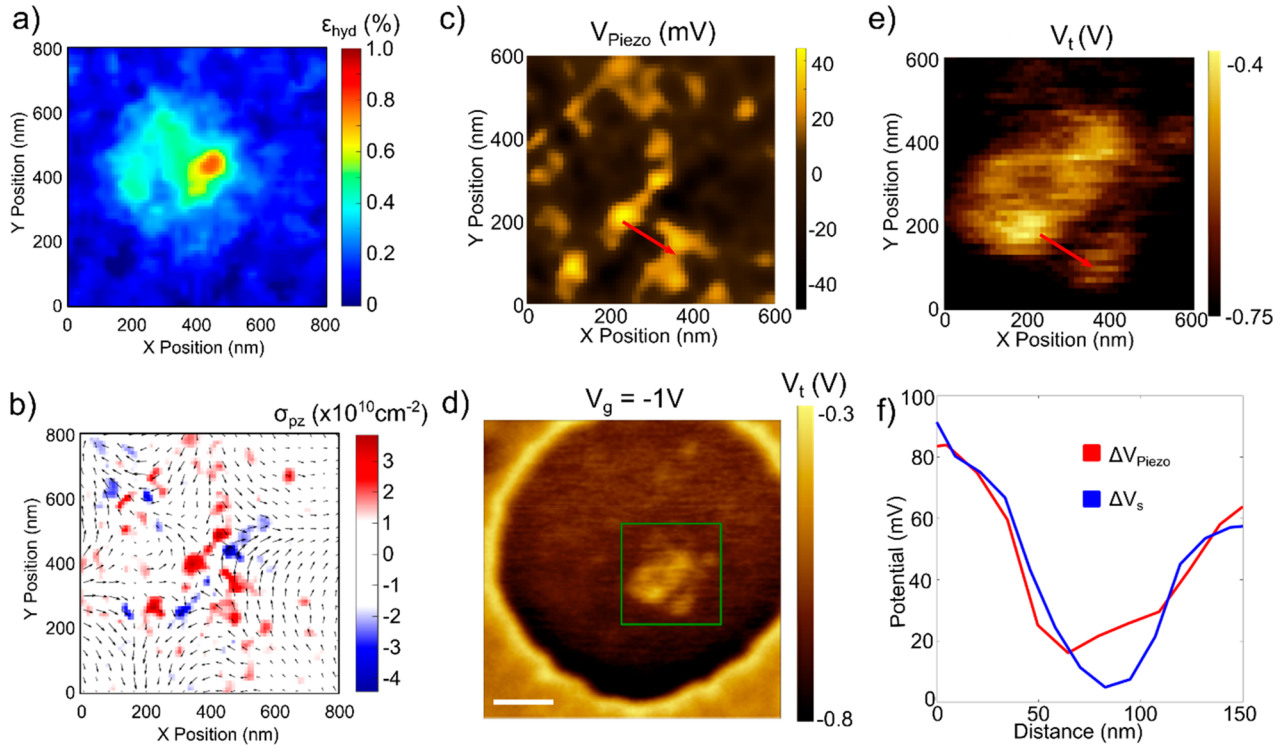

Figure 5. (a) Original hydrostatic strain derived from KPFM measurements. (b) The polarization field and resulting bound charge due to piezoelectricity, calculated from the distribution of the full strain tensor derived from the KPFM measurement. (c) Electrostatic potential due to the piezoelectric bound charge calculated assuming screening and carrier concentration $n = 8 \times 10^{10}$ cm^{-2}. (d) KPFM image of V_t at V_g = −1 V. Scale bar = 500 nm. (e) Excerpt of the KPFM data from within the green box in (c). (f) Linecut of the corrected potential variation measured by KPFM at V_g = −1 V and calculated from the piezoelectric charge distribution along the lines shown in (c,e).

https://doi.org/10.1021/acs.nanolett.3c03100
Nano Lett. 2024, 24, 1835−1842

We quantify the strain present in the monolayer using the strain deformation potentials corresponding to the conduction band of monolayer MoS_2 (Supporting Information S6).[44,45] These deformation potentials directly correspond to changes in $\Delta(E_C - E_{vac})$, which are directly related to ΔV_t^{sat} in our KPFM measurement at $V_g = 5$ V. The KPFM image at $V_g = 5$ V can therefore be converted into an image of the in-plane hydrostatic strain, which is related to the strain tensor by $\varepsilon_{hyd} = (\varepsilon_{11} + \varepsilon_{22})/2$, as shown in Figure 4b. The maximum tensile strain derived in this manner is ~0.7%, roughly centered on the nanomesa in a localized area, with a lower surrounding tensile strain of 0.2−0.4% coinciding with the area of the nanomesa. Additional tensile strain is present around the flat region of the gated MoS_2.

KPFM contrast can be influenced by a number of factors, including contamination from oligomers during the transfer process.[46] In order to verify that the KPFM contrast in Figure 5b is due to strain and not other potential sources of KPFM contrast such as contamination, the KPFM method of estimating strain is compared with a method for determining strain from the curvature of the topography measured with atomic force microscopy (AFM). Further discussion of the AFM-based method is provided in Supporting Information Section S7 and is similar to the method demonstrated by Darlington et al. for calculating strain in TMD nanobubbles.[47] The method models the mechanics of the monolayer as a thin plate undergoing large deflections. For these calculations, it is convenient to define the Airy stress function, χ:[48]

$$\sigma_{xx} = \frac{\partial^2 \chi}{\partial y^2},\ \sigma_{yy} = \frac{\partial^2 \chi}{\partial x^2},\ \sigma_{xy} = -\frac{\partial^2 \chi}{\partial x \partial y} \tag{7}$$

where σ_{xx}, σ_{yy}, and σ_{xy} represent the components of the in-plane stress tensor. The Airy stress function defined in this way represents solutions which automatically satisfy the equilibrium condition stating that the divergence of the stress tensor be equal to zero,[48] making it a useful tool for solving for stresses and strains in thin plates. An additional equation can be derived which relates the height profile of the monolayer, h, to χ and therefore the stresses and strains in thin plates:[48]

$$\nabla^4 \chi + E\left\{\frac{\partial^2 h}{\partial x^2}\frac{\partial^2 h}{\partial y^2} - \left(\frac{\partial^2 h}{\partial x \partial y}\right)^2\right\} = 0 \tag{8}$$

The curvature elements can be extracted from the AFM topography of the monolayer (Supporting Information Section S8), and solving for χ yields the in-plane stresses and strains in the monolayer according to eq 7. The in-plane hydrostatic strain distributions derived from KPFM and AFM (Figure 4c) are in good agreement, showing tensile strains of similar magnitude and position over the gated region of the MoS_2. There is more nanoscopic variation in the strain in the KPFM measurement as compared to the AFM method. We attribute this to the smoothing effect of taking second derivatives of the AFM scan. In contrast, the KPFM-FM method resolves localized strain and strain variations on smaller length scales. We show that these finer-scale variations in the strain distribution are necessary for calculating the effects of piezoelectricity in the strained MoS_2 monolayer.

The Airy stress function can also be used to convert the spatial distribution of the hydrostatic strain to a map of the complete strain tensor by recognizing from eq 7 that[48]

$$\nabla^2 \chi = \sigma_{xx} + \sigma_{yy} = \frac{2E}{1 - \upsilon}\varepsilon_{hyd} \tag{9}$$

Solving eq 9 for the Airy stress function provides a general way to calculate the full strain tensor from a known hydrostatic strain distribution. We solved eq 9 for the stress function using the hydrostatic strain distribution derived from the KPFM method. Further details are provided in Supporting Information Section S9. The result, shown in Figure 4d−g, is a spatial map of the individual components of the 2D strain tensor. This method can be useful for a variety of strain mapping techniques provided that the quantity being mapped is proportional to the in-plane hydrostatic strain. The spatial distribution of the strain tensor is relevant for understanding strain phenomena in atomically thin materials; in particular, the precise calculation of piezoelectric effects requires the strain tensor.

We next investigated piezoelectricity in the inhomogeneously strained MoS_2 monolayer using the strain tensor derived from KPFM measurements (Supporting Information S10). The piezoelectric effect generates a dielectric polarization field proportional to strain. The calculated polarization field is shown in Figure 5b. The highly inhomogeneous strain distribution results in a highly inhomogeneous polarization field, and the divergence of $\mathbf{P}$ generates a bound charge on the MoS_2 surface, σ_{pz}, given by $\sigma_{pz} = -\nabla \cdot \vec{P}$. The distribution of σ_{pz} using ε derived from the KPFM measurements is shown in Figure 5b. The magnitude of the calculated charge density is as high as 4×10^{10} e/cm^2. The piezoelectric-bound charge generates an electrostatic potential with a similar spatial distribution, as shown in Figure 5c.

The electrostatic potential due to piezoelectric-bound charges can also be detected via KPFM. We apply negative V_g to deplete the MoS_2 of free carriers, leaving the piezoelectric-bound charge. A fluctuating surface potential due to bound charges is revealed (Figure 5d), with a similar 3-fold symmetry as in the case of KPFM measurements at $V_g = 0$. There is a good match between the distribution of the calculated piezoelectric potential and V_t, as shown in Figure 5e, suggesting that the origin of the KPFM contrast at $V_g = -1$ V is largely due to piezoelectricity.

Since the monolayer is in depletion, the tip is electrically coupled to the gate rather than the MoS_2 surface, and the magnitude of the true surface potential variation measured via KPFM can be estimated according to

$$\Delta V_s = \Delta V_t \frac{C_{tg}}{C_{ts}} \tag{10}$$

where C_{tg} is the tip−gate capacitance and C_{ts} is the geometric tip−surface capacitance. Figure 5f shows a linecut of the piezoelectric potential and the corrected surface potential. There is good agreement between the calculated piezoelectric potential and the surface potential, suggesting that the origin of the surface potential variation at $V_g < 0$ V is largely due to piezoelectricity. Discrepancies between the calculated piezoelectric potential and surface potential could be due in part to the presence of contamination. The symmetry of the distribution of V_t near the nanomesa at $V_g = -1$ V is also observed at $V_g = 0$ V, suggesting that piezoelectricity is the origin of the electrostatic effect and distinct 3-fold symmetry of the surface potential near the nanomesa.

https://doi.org/10.1021/acs.nanolett.3c03100
Nano Lett. 2024, 24, 1835−1842

In conclusion, we use KPFM and electrostatic gating to measure inhomogeneous strain and its effects on monolayer MoS_2. Applying a sizable positive gate bias results in KPFM contrast generated by pinning the surface potential to the high DOS conduction band, enabling the measurement of spatial variations in the band edge energy. Combining these measurements with known strain deformation potentials enables nanoscale mapping of hydrostatic strain in monolayer MoS_2. Then, we developed a method for calculating the 2D strain tensor from the hydrostatic strain distribution. Since many experimental probes of strain in 2D materials rely on optical, electronic, or phonon energy shifts, which map strain as a scalar quantity, this method can be useful for estimating strain tensor distributions from scalar strain distributions for a variety of characterization methods. Using this analysis, we were able to calculate the piezoelectric potential generated by inhomogeneous strain and find excellent agreement with the KPFM-measured surface potential at $V_g \leq 0$ V. The ability to calculate the distribution and magnitude of the piezoelectric potential with high accuracy from the strain distribution determined via KPFM and the full 2D strain tensor demonstrates the capability of these methods for characterizing strain on the nanoscale.

■ ASSOCIATED CONTENT

Supporting Information

The Supporting Information is available free of charge at https://pubs.acs.org/doi/10.1021/acs.nanolett.3c03100.

Sample fabrication, experimental KPFM methods, details of theoretical V_t vs V_g dependence, details of strain, and piezoelectricity calculations (PDF)

■ AUTHOR INFORMATION

Corresponding Author

Edward T. Yu − *Materials Science and Engineering Program, Texas Materials Institute, University of Texas at Austin, Austin, Texas 78712, United States; Microelectronics Research Center, Department of Electrical and Computer Engineering, University of Texas at Austin, Austin, Texas 78758, United States*; Email: ety@ece.utexas.edu

Authors

Alex C. De Palma − *Materials Science and Engineering Program, Texas Materials Institute, University of Texas at Austin, Austin, Texas 78712, United States*; orcid.org/0000-0003-0857-7624

Xinyue Peng − *Department of Physics and Center for Complex Quantum Systems, University of Texas at Austin, Austin, Texas 78712, United States*

Saba Arash − *Department of Physics and Center for Complex Quantum Systems, University of Texas at Austin, Austin, Texas 78712, United States*

Frank Y. Gao − *Department of Physics and Center for Complex Quantum Systems, University of Texas at Austin, Austin, Texas 78712, United States*

Edoardo Baldini − *Department of Physics and Center for Complex Quantum Systems, University of Texas at Austin, Austin, Texas 78712, United States*

Xiaoqin Li − *Department of Physics and Center for Complex Quantum Systems, University of Texas at Austin, Austin, Texas 78712, United States*; orcid.org/0000-0002-2279-3078

Complete contact information is available at: https://pubs.acs.org/10.1021/acs.nanolett.3c03100

Author Contributions

A.C.D. and E.T.Y. conceived of the measurement and experiment. A.C.D. designed the experiment, fabricated samples, performed KPFM measurements, and performed the strain and piezoelectricity calculations. X.P., S.A., F.Y.G., E.B., and X.L. contributed the second harmonic generation measurements. All authors read and commented on the manuscript.

Notes

The authors declare no competing financial interest.

■ ACKNOWLEDGMENTS

This research was primarily supported by the National Science Foundation through the Center for Dynamics and Control of Materials: an NSF MRSEC under Cooperative Agreement Nos. DMR-1720595 and DMR-2308817. This work was performed in part at the University of Texas Microelectronics Research Center, a member of the National Nanotechnology Coordinated Infrastructure (NNCI), which is supported by the National Science Foundation (Grant ECCS-2025227), and using the facilities and instrumentation supported by the National Science Foundation through the Center for Dynamics and Control of Materials: an NSF MRSEC under Cooperative Agreement Nos. DMR-1720595 and DMR-2308817 and NSF Major Research Instrumentation (MRI) program DMR-2019130. E.B. acknowledges support from the National Science Foundation under grant DMR-2308817 (X.P.) and the Robert A. Welch Foundation under grant F-2092-20220331 (F.Y.G.).

■ REFERENCES

(1) Mas-Ballesté, R.; Gómez-Navarro, C.; Gómez-Herrero, J.; Zamora, F. 2D Materials: To Graphene and Beyond. *Nanoscale* **2011**, *3* (1), 20−30.

(2) Jariwala, D.; Sangwan, V. K.; Lauhon, L. J.; Marks, T. J.; Hersam, M. C. Emerging Device Applications for Two-Dimensional Semiconductors. *ACS Nano* **2014**, *8* (2), 1102−1120.

(3) Mueller, T.; Malic, E. Exciton Physics and Device Application of Two-Dimensional Transition Metal Dichalcogenide Semiconductors. *npj 2D Mater. Appl.* **2018**, *2* (1), 1−12.

(4) Kanungo, S.; Ahmad, G.; Sahatiya, P.; Mukhopadhyay, A.; Chattopadhyay, S. 2D Materials-Based Nanoscale Tunneling Field Effect Transistors: Current Developments and Future Prospects. *npj 2D Mater. Appl.* **2022**, DOI: 10.1038/s41699-022-00352-2.

(5) Conley, H. J.; Wang, B.; Ziegler, J. I.; Haglund, R. F.; Pantelides, S. T.; Bolotin, K. I. Bandgap Engineering of Strained Monolayer and Bilayer MoS2. *Nano Lett.* **2013**, *13* (8), 3626−3630.

(6) Frisenda, R.; Drüppel, M.; Schmidt, R.; Michaelis de Vasconcellos, S.; Perez de Lara, D.; Bratschitsch, R.; Rohlfing, M.; Castellanos-Gomez, A. Biaxial Strain Tuning of the Optical Properties of Single-Layer Transition Metal Dichalcogenides. *npj 2D Mater. Appl.* **2017**, *1* (1), 1−7.

(7) Aslan, O. B.; Deng, M.; Heinz, T. F. Strain Tuning of Excitons in Monolayer WSe2. *Phys. Rev. B* **2018**, *98* (11), No. 115308.

(8) Wang, F.; Li, S.; Bissett, M. A.; Kinloch, I. A.; Li, Z.; Young, R. J. Strain Engineering in Monolayer WS 2 and WS 2 Nanocomposites. *2D Mater.* **2020**, *7*, 045022.

(9) Castellanos-Gomez, A.; Roldán, R.; Cappelluti, E.; Buscema, M.; Guinea, F.; Van Der Zant, H. S. J.; Steele, G. A. Local Strain Engineering in Atomically Thin MoS2. *Nano Lett.* **2013**, *13* (11), 5361−5366.

(10) Bertolazzi, S.; Brivio, J.; Kis, A. Stretching and Breaking of Ultrathin MoS 2. *ACS Nano* **2011**, *5* (12), 9703−9709.
(11) Zhang, R.; Koutsos, V.; Cheung, R. Elastic Properties of Suspended Multilayer WSe2. *Appl. Phys. Lett.* **2016**, DOI: 10.1063/1.4940982.
(12) Nemes-Incze, P.; Kukucska, G.; Koltai, J.; Kürti, J.; Hwang, C.; Tapasztó, L.; Biró, L. P. Preparing Local Strain Patterns in Graphene by Atomic Force Microscope Based Indentation. *Sci. Rep.* **2017**, *7* (1), 1−7.
(13) Niu, T.; Cao, G.; Xiong, C. Indentation Behavior of the Stiffest Membrane Mounted on a Very Compliant Substrate: Graphene on PDMS. *Int. J. Solids Struct.* **2018**, *132*−*133*, 1−8.
(14) Darlington, T. P.; Carmesin, C.; Florian, M.; Yanev, E.; Ajayi, O.; Ardelean, J.; Rhodes, D. A.; Ghiotto, A.; Krayev, A.; Watanabe, K.; Taniguchi, T.; Kysar, J. W.; Pasupathy, A. N.; Hone, J. C.; Jahnke, F.; Borys, N. J.; Schuck, P. J. Imaging Strain-Localized Excitons in Nanoscale Bubbles of Monolayer WSe2 at Room Temperature. *Nat. Nanotechnol.* **2020**, *15* (10), 854−860.
(15) Chaste, J.; Missaoui, A.; Huang, S.; Henck, H.; Ben Aziza, Z.; Ferlazzo, L.; Naylor, C.; Balan, A.; Johnson, A. T. C.; Braive, R.; Ouerghi, A. Intrinsic Properties of Suspended MoS2 on SiO2/Si Pillar Arrays for Nanomechanics and Optics. *ACS Nano* **2018**, *12* (4), 3235−3242.
(16) Palacios-Berraquero, C.; Kara, D. M.; Montblanch, A. R. P.; Barbone, M.; Latawiec, P.; Yoon, D.; Ott, A. K.; Loncar, M.; Ferrari, A. C.; Atatüre, M. Large-Scale Quantum-Emitter Arrays in Atomically Thin Semiconductors. *Nat. Commun.* **2017**, DOI: 10.1038/ncomms15093.
(17) Zhang, Z.; De Palma, A. C.; Brennan, C. J.; Cossio, G.; Ghosh, R.; Banerjee, S. K.; Yu, E. T. Probing Nanoscale Variations in Strain and Band Structure of Mo S2 on Au Nanopyramids Using Tip-Enhanced Raman Spectroscopy. *Phys. Rev. B* **2018**, *97* (8), 1−10.
(18) Milovanović, S. P.; Covaci, L.; Peeters, F. M. Strain Fields in Graphene Induced by Nanopillar Mesh. *J. Appl. Phys.* **2019**, DOI: 10.1063/1.5074182.
(19) Duerloo, K. A. N.; Ong, M. T.; Reed, E. J. Intrinsic Piezoelectricity in Two-Dimensional Materials. *J. Phys. Chem. Lett.* **2012**, *3* (19), 2871−2876.
(20) Zhu, H.; Wang, Y.; Xiao, J.; Liu, M.; Xiong, S.; Wong, Z. J.; Ye, Z.; Ye, Y.; Yin, X.; Zhang, X. Observation of Piezoelectricity in Free-Standing Monolayer MoS2. *Nat. Nanotechnol.* **2015**, *10* (2), 151−155.
(21) Wu, W.; Wang, L.; Li, Y.; Zhang, F.; Lin, L.; Niu, S.; Chenet, D.; Zhang, X.; Hao, Y.; Heinz, T. F.; Hone, J.; Wang, Z. L. Piezoelectricity of Single-Atomic-Layer MoS2 for Energy Conversion and Piezotronics. *Nature* **2014**, *514* (7253), 470−474.
(22) Rostami, H.; Guinea, F.; Polini, M.; Roldán, R. Piezoelectricity and Valley Chern Number in Inhomogeneous Hexagonal 2D Crystals. *npj 2D Mater. Appl.* **2018**, *2* (1), 28−30.
(23) Wang, W.; Zhou, L.; Hu, S.; Novoselov, K. S.; Cao, Y. Visualizing Piezoelectricity on 2D Crystals Nanobubbles. *Adv. Funct. Mater.* **2021**, *31* (6), 1−7.
(24) Ares, P.; Cea, T.; Holwill, M.; Wang, Y. B.; Roldán, R.; Guinea, F.; Andreeva, D. V.; Fumagalli, L.; Novoselov, K. S.; Woods, C. R. Piezoelectricity in Monolayer Hexagonal Boron Nitride. *Adv. Mater.* **2020**, DOI: 10.1002/adma.201905504.
(25) Ahn, G. H.; Amani, M.; Rasool, H.; Lien, D. H.; Mastandrea, J. P.; Ager, J. W.; Dubey, M.; Chrzan, D. C.; Minor, A. M.; Javey, A. Strain-Engineered Growth of Two-Dimensional Materials. *Nat. Commun.* **2017**, *8* (1), 1−7.
(26) Cordovilla Leon, D. F.; Li, Z.; Jang, S. W.; Cheng, C. H.; Deotare, P. B. Exciton Transport in Strained Monolayer WSe 2. *Appl. Phys. Lett.* **2018**, DOI: 10.1063/1.5063263.
(27) Liu, X.; Sachan, A. K.; Howell, S. T.; Conde-Rubio, A.; Knoll, A. W.; Boero, G.; Zenobi, R.; Brugger, J. Thermomechanical Nanostraining of Two-Dimensional Materials. *Nano Lett.* **2020**, *20* (11), 8250−8257.
(28) Colangelo, F.; Morandi, A.; Forti, S.; Fabbri, F.; Coletti, C.; Di Girolamo, F. V.; Di Lieto, A.; Tonelli, M.; Tredicucci, A.; Pitanti, A.; Roddaro, S. Local Tuning of WS2 Photoluminescence Using Polymeric Micro-Actuators in a Monolithic van Der Waals Heterostructure. *Appl. Phys. Lett.* **2019**, *115* (18), 1−5.
(29) Lyu, B.; Li, H.; Jiang, L.; Shan, W.; Hu, C.; Deng, A.; Ying, Z.; Wang, L.; Zhang, Y.; Bechtel, H. A.; Martin, M. C.; Taniguchi, T.; Watanabe, K.; Luo, W.; Wang, F.; Shi, Z. Phonon Polariton-Assisted Infrared Nanoimaging of Local Strain in Hexagonal Boron Nitride. *Nano Lett.* **2019**, *19* (3), 1982−1989.
(30) Luo, S.; Hao, G.; Fan, Y.; Kou, L.; He, C.; Qi, X.; Tang, C.; Li, J.; Huang, K.; Zhong, J. Formation of Ripples in Atomically Thin MoS2 and Local Strain Engineering of Electrostatic Properties. *Nanotechnology* **2015**, *26* (10), 105705.
(31) Kwon, S.; Kwon, M. H.; Song, J.; Kim, E.; Kim, Y.; Kim, B. R.; Hyun, J. K.; Lee, S. W.; Kim, D. W. Light-Induced Surface Potential Modification in MoS2Monolayers on Au Nanostripe Arrays. *Sci. Rep.* **2019**, *9* (1), 1−6.
(32) Alexeev, E. M.; Mullin, N.; Ares, P.; Nevison-Andrews, H.; Skrypka, O.; Godde, T.; Kozikov, A.; Hague, L.; Wang, Y.; Novoselov, K. S.; Fumagalli, L.; Hobbs, J. K.; Tartakovskii, A. I. Emergence of Highly Linearly Polarized Interlayer Exciton Emission in MoSe2/WSe2Heterobilayers with Transfer-Induced Layer Corrugation. *ACS Nano* **2020**, *14* (9), 11110−11119.
(33) Nonnenmacher, M.; O'Boyle, M. P.; Wickramasinghe, H. K. Kelvin Probe Force Microscopy. *Appl. Phys. Lett.* **1991**, *58* (25), 2921−2923.
(34) Büttiker, M.; Thomas, H.; Prêtre, A. Mesoscopic Capacitors. *Phys. Lett. A* **1993**, *180* (4−5), 364−369.
(35) Roelofs, W. S. C.; Mathijssen, S. G. J.; Janssen, R. A. J.; De Leeuw, D. M.; Kemerink, M. Accurate Description of Charge Transport in Organic Field Effect Transistors Using an Experimentally Extracted Density of States. *Phys. Rev. B - Condens. Matter Mater. Phys.* **2012**, *85* (8), 1−6.
(36) Halpern, E.; Cohen, G.; Gross, S.; Henning, A.; Matok, M.; Kretinin, A. V.; Shtrikman, H.; Rosenwaks, Y. Measuring Surface State Density and Energy Distribution in InAs Nanowires. *Phys. Status Solidi Appl. Mater. Sci.* **2014**, *211* (2), 473−482.
(37) Wagner, T.; Köhler, D.; Milde, P.; Eng, L. M. Probing the Local Surface Potential and Quantum Capacitance in Single and Multi-Layer Graphene. *Appl. Phys. Lett.* **2013**, DOI: 10.1063/1.4813076.
(38) Wang, K. C.; Stanev, T. K.; Valencia, D.; Charles, J.; Henning, A.; Sangwan, V. K.; Lahiri, A.; Mejia, D.; Sarangapani, P.; Povolotskyi, M.; Afzalian, A.; Maassen, J.; Klimeck, G.; Hersam, M. C.; Lauhon, L. J.; Stern, N. P.; Kubis, T. Control of Interlayer Physics in 2H Transition Metal Dichalcogenides. *J. Appl. Phys.* **2017**, DOI: 10.1063/1.5005958.
(39) Fang, N.; Nagashio, K. Band Tail Interface States and Quantum Capacitance in a Monolayer Molybdenum Disulfide Field-Effect-Transistor. *J. Phys. D. Appl. Phys.* **2018**, *51* (6), 24−26.
(40) Shakya, J.; Kumar, S.; Kanjilal, D.; Mohanty, T. Work Function Modulation of Molybdenum Disulfide Nanosheets by Introducing Systematic Lattice Strain. *Sci. Rep.* **2017**, *7* (1), 1−9.
(41) Lanzillo, N. A.; Simbeck, A. J.; Nayak, S. K. Strain Engineering the Work Function in Monolayer Metal Dichalcogenides. *J. Phys.: Condens. Matter* **2015**, *27* (17), 175501.
(42) Buscema, M.; Steele, G. A.; van der Zant, H. S. J.; Castellanos-Gomez, A. The Effect of the Substrate on the Raman and Photoluminescence Emission of Single-Layer MoS2. *Nano Res.* **2014**, *7* (4), 561−571.
(43) Lu, C.; Li, G.; Mao, J.; Wang, L.; Andrei, E. Y. Bandgap, Mid-Gap States, and Gating Effects in MoS 2. *Nano Lett.* **2014**, *14*, 4628−4633.
(44) Van De Walle, C. G.; Martin, R. M. Absolute Deformation Potentials: Formulation and Ab Initio Calculations for Semiconductors. *Phys. Rev. Lett.* **1989**, *62* (17), 2028−2031.
(45) Wiktor, J.; Pasquarello, A. Absolute Deformation Potentials of Two-Dimensional Materials. *Phys. Rev. B* **2016**, *94* (24), 1−8.
(46) Glasmästar, K.; Gold, J.; Andersson, A.-S.; Sutherland, D. S.; Kasemo, B. Silicone Transfer during Microcontact Printing. *Langmuir* **2003**, *19* (13), 5475−5483.

https://doi.org/10.1021/acs.nanolett.3c03100
Nano Lett. 2024, 24, 1835−1842

(47) Darlington, T. P.; Krayev, A.; Venkatesh, V.; Saxena, R.; Kysar, J. W.; Borys, N. J.; Jariwala, D.; Schuck, P. J. Facile and Quantitative Estimation of Strain in Nanobubbles with Arbitrary Symmetry in 2D Semiconductors Verified Using Hyperspectral Nano-Optical Imaging. *J. Chem. Phys.* **2020**, DOI: 10.1063/5.0012817.
(48) Landau, L. D.; Kosevich, A. M.; Pitaevskii, L. P.; Lifshitz, E. M. *Theory of Elasticity*, 3rd ed.; Butterworth-Heinemann, 1986.

https://doi.org/10.1021/acs.nanolett.3c03100
Nano Lett. 2024, 24, 1835−1842